NANO LETTERS

2007
Vol. 7, No. 7
1869−1877

Direct Nanoimprinting of Metal Nanoparticles for Nanoscale Electronics Fabrication

Seung H. Ko,[†,‡] Inkyu Park,[†,§] Heng Pan,[‡] Costas P. Grigoropoulos,[*,‡] Albert P. Pisano,[§] Christine K. Luscombe,[||,⊥] and Jean M. J. Fréchet[||]

Department of Mechanical Engineering, University of California, Berkeley, California 94720-1740, Berkeley Sensor and Actuator Center (BSAC), University of California, Berkeley, California 94720-1774, and Department of Chemistry, University of California, Berkeley, California 94720-1460

Received February 10, 2007; Revised Manuscript Received May 3, 2007

ABSTRACT

One-step direct nanoimprinting of metal nanoparticles was investigated to fabricate nano-/microscale metallic structures such as nanodot and nanowire arrays. This was done at low temperatures and pressures, utilizing the low melting temperature and viscosity of metal nanoparticle solutions. Through precise control of the fluidic properties of the nanoparticle solution and the mold design, high-quality nanoscale features with no or negligible residual layer were nanoimprinted. Nanoscale electronic devices were also demonstrated, including nanowire resistors and nanochannel organic field effect transistors with an air-stable semiconducting polymer.

Nanoimprinting lithography (NIL) is emerging as an alternative nanopatterning technology to traditional photolithography that allows the fabrication of two-dimensional or three-dimensional structures with submicrometer resolution and the patterning and modification of functional materials. Its major advantages are low-cost, high-throughput production of various nanostructures with operational ease. NIL has been applied in various fields such as biological nanodevices,[1] nanophotonic devices (gratings and photonic crystal structures),[2,3] organic electronics,[4−6] and the patterning of magnetic materials.[7]

In nanoimprinting, a mold with nanostructures is pressed to deform and shape a thin material film deposited on a substrate. Therefore, to achieve successful nanoimprinting, the material needs to have proper flow properties (e.g., viscosity and surface tension) adjustable for complete mold pattern replication within reasonable processing temperatures and pressures. For nanoimprinting, materials with low viscosities are desirable and usually are either thermoplastics (e.g., poly(methyl methacrylate), PMMA), thermoset polymers,[8] UV-curable polymers,[9,10] or other deformable materials with the desired flow properties. The imprinting material flow is usually achieved by heating to a temperature at which the materials exhibit liquid or viscoelastic behavior.[11,12] However, nanoimprinting for metals is significantly harder to achieve due to their high melting temperature. Metal nanoimprinting is typically an indirect process where a polymer (e.g., PMMA) pattern is first created by nanoimprinting, which is then used as mask for dry etching of a predeposited metal film or as part of the metal lift-off process.[11] As one can see, conventional metal nanoimprinting involves multiple steps and expensive processes, thereby increasing the cost of manufacturing and offsetting the advantages of the nanoimprinting process. Very few direct metal nanoimprinting processes have been demonstrated so far due to the high melting temperature of metals. As alternatives to metal direct nanoimprinting, a few solid-state embossing methods based on plastic deformation of metal thin films have been introduced. These approaches involved either deformation of metal film under very high pressure[13] or deformation of a metal thin film/polymer multilayer under lower pressure.[14] Evidently, these processes are limited by the fact that the metal is still in the solid state. Either ultrahigh pressures or metal/polymer multilayers and sharp mold geometries are required to deform the metallic layer. Additionally, these methods do not allow the fabrication of isolated, arbitrary features, and always leave unwanted residual polymer layers. For the process to be useful for a

* Corresponding author. E-mail: cgrigoro@me.berkeley.edu.
† These authors equally contributed to this work.
‡ Department of Mechanical Engineering, University of California, Berkeley.
§ Berkeley Sensor and Actuator Center (BSAC), University of California, Berkeley.
|| Department of Chemistry, University of California, Berkeley.
⊥ Current address: Materials Science and Engineering Department, University of Washington, Seattle, WA 98195-2120.

10.1021/nl070333v CCC: $37.00 © 2007 American Chemical Society
Published on Web 06/05/2007

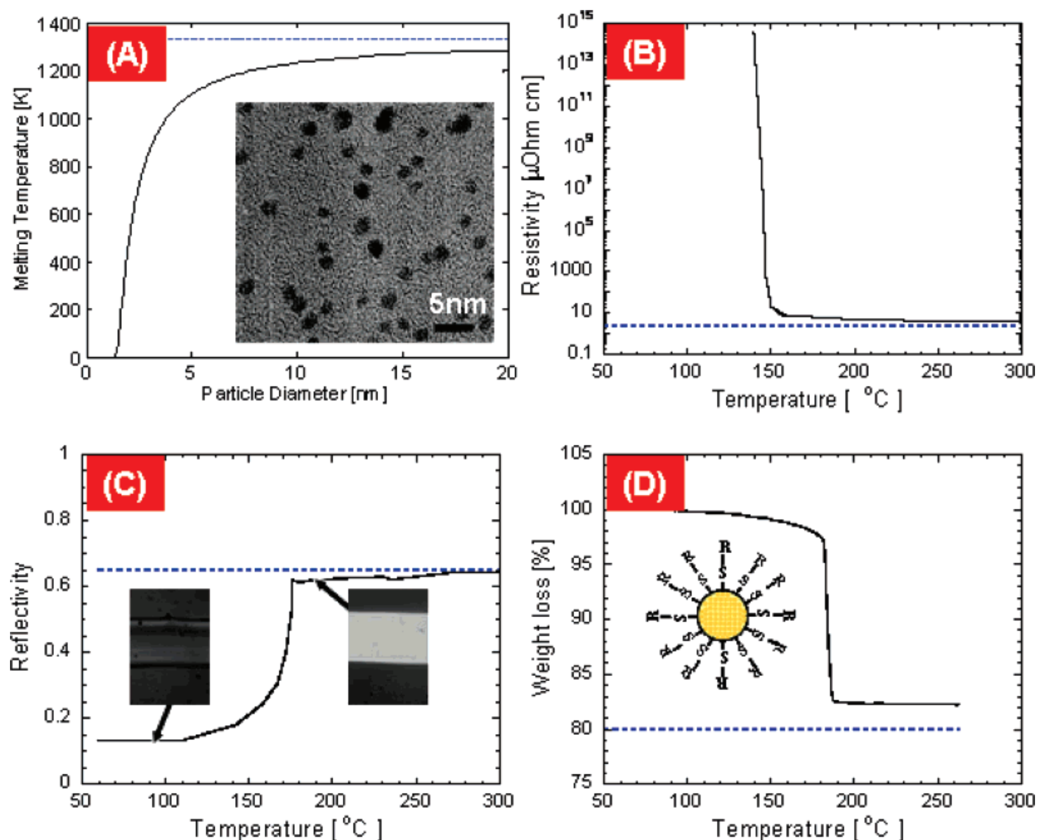

Figure 1. Thermal (melting) characteristics of SAM-protected nanoparticles. (A) Melting temperature of gold nanoparticles with different size calculated from the equation.[37] Inset is the TEM picture of nanoparticles. Dotted line represents bulk gold melting temperature (1336 K). (B) Resistivity (dotted line represents bulk gold resistivity (2.65 $\mu\Omega$·cm)). (C) Reflectivity at 514.5 nm wavelength. Dotted line represents bulk gold reflectivity (0.65) and insets represent the optical images of nanoparticle film before (left) and after (right) the nanoparticle melting. (D) Mass change (measured by Seiko Instruments SSC 5200 TG/DTA 220 in nitrogen environment) at various heating temperatures. Inset is the schematic representation of a single nanoparticle with SAM. Dotted line represents the theoretical mass percentage of gold in gold nanoparticles.

larger number of applications, liquid-based material nanoimprinting is more ideal.

In this paper, we demonstrate a novel metal direct nanoimprinting method based on the utilization of a metallic material in the form of a nanoparticle solution. This process eliminates the need of intermediate polymer nanoimprinting steps for dry etching or vacuum deposition. Here, a metal nanoparticle solution was effectively used as a precursor to use the solution processable form of the metal component for the nanoimprinting process, thereby eliminating the need to exceed the bulk metal melting temperature. The nanoimprinted nanoparticles can be transformed into conductive and continuous metal films by low-temperature nanoparticle melting. This approach offers the considerable advantage of using low temperatures and pressures, which can be potentially applied to flexible substrate electronics.

Direct metal nanoimprinting is a new method that simplifies the manufacturing process and allows potential applications that are not compatible with photoresist or solvent chemistry. It allows simultaneous large-scale definition of metallic patterns with superior resolution, ranging from several millimeters down to nanometer scales less than 150 nm. In addition to being time and cost efficient, the process enables creation of smaller features compared with other direct printing techniques such as inkjet printing,[16−18] screen printing,[19] laser-induced forward transfer,[20] and thermal imaging,[21] which can provide only limited resolution down to 20−50 μm.

Nanomaterials exhibit remarkable specific properties due to their large surface to volume ratio, large surface energy, and spatial confinement, which cannot be observed in bulk materials. Metal nanoparticles show large melting temperature depression due to the thermodynamic size effect.[22,23] Compared to the melting temperature of bulk gold (1063 °C), 2−3 nm sized gold nanoparticles start to melt at around 130−140 °C, a range that is compatible with flexible polymer substrates (Figure 1A). The metal nanoparticles can be transformed from an insulator to a conductor after energy input by heating on a hot plate or via laser irradiation. The gold nanoparticles used in this study were encapsulated with a hexanethiol self-assembled monolayer (SAM) and were synthesized using a two-phase reduction method.[24] Details of the synthesis can be found in the Supporting Information. The size of the synthesized nanoparticles is distributed in the range of 1−3 nm as measured by transmission electron microscopy (TEM) (Figure 1A, inset). The thermal (melting) characteristics of nanoparticles were investigated at various heating temperatures on a hot plate. When the melting starts, the nanoparticles experience significant effects, such as dramatic change in the electrical resistivity (Figure 1B),

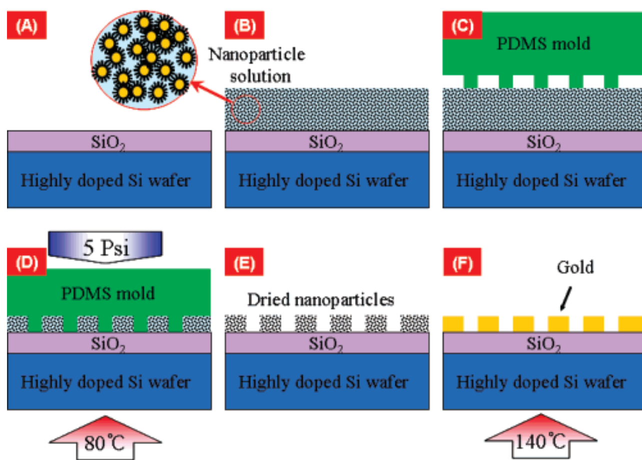

Figure 2. Nanoparticle nanoimprinting process. (A, B) Dispensing nanoparticle solution on SiO_2/P+ Si wafer. (C, D) Pressing PDMS nanoimprinting mold on nanoparticle solution under 5 psi pressure at 80 °C. (E, F) Removal of mold and induce nanoparticle melting on hot plate at 140 °C. The magnified view shows the SAM-protected nanoparticles suspended in organic solvent.

reflectance (Figure 1C), and mass (Figure 1D) around at 140−150 °C where the SAMs start to desorb and evaporate from the nanoparticles.

The SAM-protected nanoparticles were suspended in an α-terpineol carrier solvent (10 wt %). The SAM is critical for nanoparticles because it not only controls the size of the nanoparticles but also enhances the stability of the nanoparticles dispersed in solvents. This metal nanoparticle solution improves processing conditions by allowing low temperature solution processing of the metal components and is the basis for our direct metal nanoimprinting.

Our nanoimprinting process consists of the following steps: (i) the metal nanoparticle solution is dispensed on a SiO_2/P+ Si wafer; (ii) the deposit is imprinted using a poly(dimethylsiloxane) (PDMS) mold; and (iii) the patterned nanoparticles are melted on a hot plate. Figure 2 describes the metal nanoparticle nanoimprinting process. First, highly doped p-type silicon wafer (Silicon Materials Inc. $\rho < 0.005$ Ω·cm) which was oxidized to form 100 nm of thermal SiO_2 by wet oxidation at 900 °C for 37 min (Figure 2A) was prepared and cleaned using piranha solution (~50 parts 96% H_2SO_4 :1 part 30% H_2O_2 at 120 °C). This SiO_2/P+ Si wafer structure is used as a dielectric/gate structure for transistors. The gold nanoparticles encapsulated by SAM in an α-terpineol solvent (0.1 mL) were dispensed on top of the SiO_2/P+ Si wafer which was maintained at 80 °C. The pattern replication was optimized at this temperature, where the pattern replication showed the best result with minimal residual layer. This temperature may cause favorable solution viscosity and surface tension for nanoimprinting process. The PDMS mold was applied on top of a nanoparticle solution with a small pressure (5 psi) by a laboratory-built nanoimprinting system with a digital load cell and a feedback controlled heating stage. (Figure 2C,D). The substrate was heated at 80 °C for 10 min to allow the nanoparticle solution to fill the mold and to evaporate the organic solvent. The substrate was then cooled down to room temperature for 50 min (to ensure complete cooling) and the PDMS mold was carefully removed from the substrate (Figure 2E). Finally, the nanoimprinted sample was heated on a hot plate at 140 °C to induce nanoparticle melting to transform collections of nanoparticles into a continuous conducting film (Figure 2F).

A PDMS mold was used instead of hard mold (e.g., silicon or quartz) because it can be easily replicated from an original silicon master and since it also allows evaporation of organic solvents and greatly contributes to the residual layer minimization due to the great conformal contact between the PDMS mold and the substrate[25] during the nanoimprinting process. Detailed fabrication process of the PDMS mold can be found in the Supporting Information. Metal nanoparticles carried by liquid solvents have several advantages over dry or aerosol state nanoparticles by providing much greater processing flexibility.[26] The most critical properties for successful imprinting are viscosity and surface tension of the solution.[11,27] α-Terpineol has a very wide viscosity range from a very high viscosity (almost a solid) at room temperature to a low viscosity fluid (~10 cP) at 100 °C. Moderate heating during the nanoimprinting process allows the nanoparticle solution to attain low viscosity. This, along with the conformal PDMS mold−substrate surface contact, facilitates the complete pattern replication with minimal residual layer. Cooling after pattern formation prevents the imprinted structure from collapsing during the demolding step because of the high viscosity of the solution at room temperature. The imprinting processing temperature was optimized to achieve the best filling of the solution into the PDMS molds. This was done by balancing the two events that alter the viscosity of the solution: first, the decrease in viscosity that occurs with increasing temperature, and second, the simultaneous increase in viscosity that takes place because of solvent evaporation at elevated temperatures. The optimum temperature was found to be 80 °C. Since the specific nanoparticle material does not alter significantly the fluidic properties of the nanoparticle solution, the nanoimprinting process developed in this work is quite versatile and hence can be used for a variety of metallic nanoparticles. Furthermore, the technique can be easily applicable to a broad range of functional molecules and nanoparticle materials with minimal process modification.

Direct nanoimprinting of diverse gold structures, such as nanodot, nanowire, and serpentine nanowire arrays with varying sizes (down to 100 nm), densities, and aspect ratios is shown in Figure 3. Figure 3A shows optical darkfield microscope images of arrays of 200 nm (panel A, parts ii, iv, and v, 400 nm pitch) and 400 nm (panel A, parts i, iii, and vi, 800 nm pitch) sized nanodots with three different shapes (panel A, parts i and iv, circular; panel A, parts ii and iii, diamond; panel A, parts v and vi, square). While 400 nm dot arrays are clearly visible, 200 nm dots could not be easily observed at the same illumination light intensity because smaller dots scatter less light. The atomic force microscopy (AFM) topography images of the nanodot arrays are shown in Figure 3B. Arrays of square-shaped (Figure 3B(i, iii)) and circular-shaped (Figure 3B(ii)) nanodots of

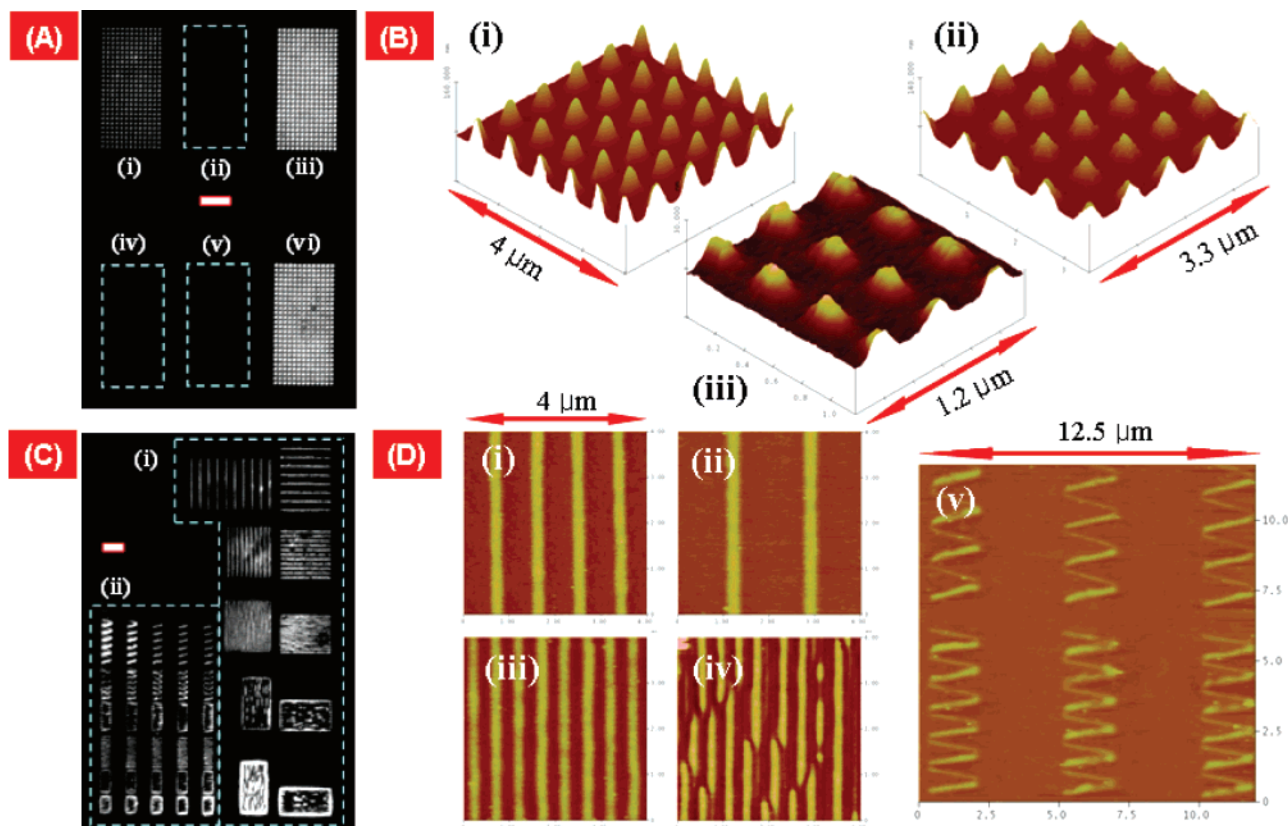

Figure 3. Nanoimprinted gold nanofeatures. Optical dark field images of (A) nanodots and (C) nanowires (inset scale bar corresponds to 5 μm). AFM topography images of (B) nanodots, (D(i−iv)) straight nanowires, and (D(v)) serpentine nanowires.

width in the range of 130−250 nm (fwhm) with heights of 8−50 nm depending upon the width were successfully fabricated by nanoimprinting. The lateral feature size on the PDMS stamp was slightly larger than those of imprinted structures by maximum 10%, and the depth was between 40 and 50 nm. Precise control of localization and pattern replication were achieved with high fidelity and negligible or no residual layer. In parts C and D of Figure 3 are shown one-dimensional nanowires made by nanoimprinting. Figure 3C shows optical darkfield microscope images of 100 nm wide (nominal) nanowire arrays with different pitch (panel C, part i, 200/300/500/900/1700 nm pitch from the bottom) and serpentine nanowires (panel A, part ii, 24 μm total length). The AFM topography images of the nanowire arrays are shown in Figure 3D. Nanowire arrays with relatively larger pitch (down to 300 nm pitch) can imprint 200 nm (fwhm) clean nanowires without discontinuity (Figure 3D, parts i−iii). However, 200 nm pitch nanowire imprinting (Figure 3D, part iv) shows local line discontinuities that may be a result of incomplete filling at the nanoscale, the line width broadening by possibly material diffusive spreading and expansion of trapped air or moisture.[12] This is more serious when the line width becomes comparable with the pitch. This pattern expansion limits the pattern density and reduces resolution. Besides straight nanowires, meandering nanowires (Figure 3D, part v) were printed successfully without discontinuity.

After the nanoimprinted metal nanoparticles are melted and sintered on a hot plate, the nanofeatures show tapered sidewalls and vertical shrinkage compared to feature depths of the PDMS mold. These may be due to either reflow of the nanoparticle solution and densification during the melting process, incomplete filling of metal nanoparticle solution into the PDMS mold, or deformation of PDMS mold by the applied pressure. Similar influence of densification and Poisson's ratio of nanoimprinted polymers on the cross section of the fabricated features has been reported.[11,28] Significant deviation in the sidewall angle from vertical can change the line width during the nanoparticle melting. As the aspect ratio becomes small, the sidewall angle degradation becomes more severe for the isolated dots than for the nanowire features. The maximum aspect ratio that can be obtained is highly dependent on the size and shape of the features. In this work, we could obtain aspect ratios as large as 1/3 (height/width) from the master pattern with 1/1.7 aspect ratio. Because of the compressive deformation of elastomeric mold material (PDMS), the aspect ratio decreased in the case of small or isolated structures.

The imprinting of large and isolated array features surrounded by large unstructured areas is challenging in terms of complete filling of the fluid in the PDMS mold and minimizing the residual layer.[11,27] This is true for either elevated features or cavities and becomes more critical as the size becomes smaller. We strived to solve this problem by designing microscale dummy features near the active nanoscale structures and by dispensing precise quantities of the nanoparticle solution. This could help both minimize residual layers and achieve uniform filling of nanoparticle

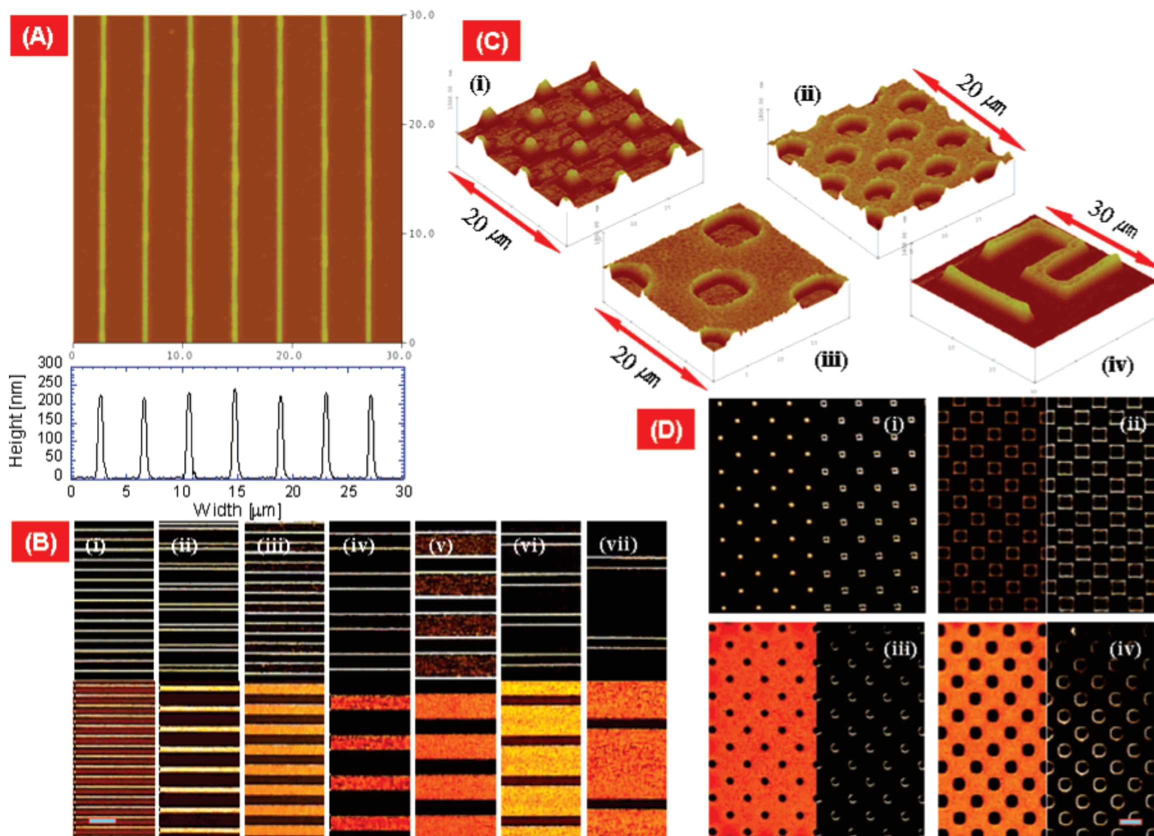

Figure 4. Nanoimprinted gold nano-/microfeatures. AFM topography images of (A) nanowire arrays, (C, i) positive microdot arrays, (C, ii, iii) negative microdot arrays, and (C, iv) letters. Optical images of (B) microwire arrays (top row, dark field; bottom row, bright field), (D, i, ii) positive microdots, and (D, iii, iv) negative microdots (left column, dark field; right row, bright field). Inset scale bars correspond to 10 μm.

solutions in the nanoscale features across the entire imprinting mold area. The residual layers were analyzed by energy dispersive X-ray analysis, electrical measurement, optical image, and AFM scanning. These diagnostics showed absence of residual layer in the imprinted area. In particular, electrical measurements assured that neighboring nanowires are electrically isolated, thereby proving that there are no continuous and conductive left-over residual layers that may cause leakage current.

Micro-/nanometer size Au lines and positive and negative Au dots were fabricated by nanoimprinting. AFM images and cross sections of nanowires with 450 nm width (fwhm, 4 μm pitch) and 280 nm height are shown in Figure 4A. Optical dark field/bright field microscope images of microwires of various widths and pitch are presented in Figure 4B (1/2/4/6/12/14/30 μm line with and 4/8/8/16/16/16/32 μm pitch from i to vii; 300 nm high; darkfield, top row; bright field, bottom row). The AFM topography images (Figure 4C) and optical darkfield (left half) and bright field (right half) microscope images (Figure 4D) of imprinted positive and negative micrometer-sized features are shown. Square positive features (from negative mold) of diverse size and density are shown (Figure 4C, part i, 2.7 μm width and 8 μm pitch; Figure 4D, parts i and ii, 3/6 μm width and 16 μm pitch, 200 nm high). On the other hand, a variety of square and circular negative features (from positive mold) is presented (Figure 4C, parts ii and iii, 2.4/4.6 μm width and 8/16 μm pitch; Figure 4D, parts iii and iv, 3/6 μm width and 16 μm pitch, 200 nm high).

The low viscosity guarantees efficient transport of the solution inside the cavities of the mold, enabling equivalent results for both positive and negative features. It is known that the feature size and the positive/negative conformation of the mold have a drastic influence on the imprinting of high viscosity polymers and make the negative mold conformation more difficult to replicate.[29] However, partially filled structures are observed in imprinted large and dense isolated positive features (Figure 4D, part ii). This may be due to the volume shrinkage, solvent evaporation, and trapped air. In contrast, imprinted line features (Figure 4B) did not show such problems. This partially filled cavity is usually observed in the viscous flow of thin PMMA film into the microcavities during the hot embossing lithography.[15] The step heights of the imprinted nanoparticle features are found to be functions of the shape and dimensions of the original features on the PDMS mold. Also, it should be noted that the features have elevated ridges. This is the so-called "rabbit-ear" effect[30] that is probably due to incomplete filling of nanoparticle solution in the mold and wetting around the surface of the mold. The size-dependence and rabbit-ear effects are shown in Figure 5B, where the data were taken from the AFM scanning images of gold line arrays imprinted from PDMS molds of different width (2/4/6/8/10/12/14/16/18/20/30 μm) but the same depth (1.2 μm). As the feature

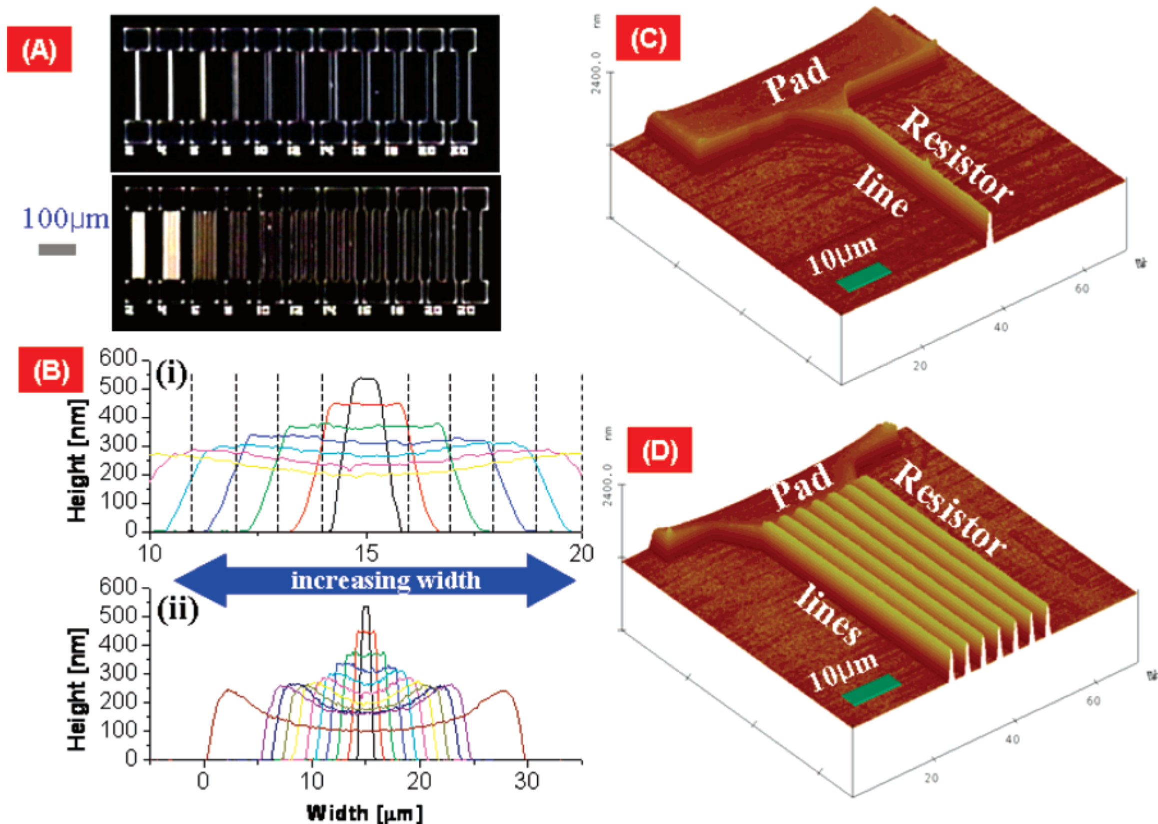

Figure 5. Nanoimprinted gold resistors. (A) Optical dark field images of (i) single and (ii) multiline resistors. Inset scale bar corresponds to 100 μm. (B) AFM cross section images of single gold resistors with diverse widths and (i) magnified view. Dotted lines represent the sidewalls of the PDMS mold. The initial height of the PDMS mold without any loading is 1.2 μm. AFM topography image of (C) a single line resistor and (D) a multiple line resistor. Inset scale bar corresponds to 10 μm.

size is increased, the feature height is decreased, and the rabbit-ear effect becomes more significant relative to the feature height. Gravity becomes important beyond a particular length scale (κ^{-1}, capillary length). This can be estimated by comparing the Laplace pressure (γ/κ^{-1}) to the hydrostatic pressure ($\rho g \kappa^{-1}$) where γ is the surface tension, ρ is the liquid density, and g is gravitational acceleration.[31] The characteristic length ($2\kappa^{-1}$) was found to be approximately 8 μm. Gravity is negligible for sizes $r < \kappa^{-1}$ (4 μm) in the capillary dominated regime. Cross sectional shapes with elevated edges and flat, lowered center tend to be produced in the capillary and gravity regimes, respectively. When the channel width is comparable or smaller than twice the capillary length (8 μm), the capillary effect from the mold side walls dominates over the entire channel and consequently flatter surfaces of larger height are imprinted.

The electrical properties of the nanoimprinted features are crucial for the eventual use in micro-/nanoelectronics applications. Two types of resistivity test configurations—single line resistors as shown in Figure 5A, part i (optical dark field image), and Figure 5C (AFM image) and multiple line resistors as shown in Figure 5A, part ii (optical dark field image), and Figure 5D (AFM image)—were fabricated by direct nanoimprinting. The resistivity (ρ) is calculated from RA/L. The resistance R was measured with a microneedle probe station. A is the cross sectional area of the gold line measured from AFM scanning data, and L the length of the test sample (200 μm). The measured resistivity (30 $\mu\Omega$·cm) obtained from nanoimprinting was almost 1 order higher than the bulk value (2.65 $\mu\Omega$·cm, solid line in Figure 1B), but it was still sufficiently conductive for high-performance electronics. This resistivity value difference could be explained by enhanced carrier scattering in the presence of a polycrystalline structure, rough surface ($R_{rms} \sim 5$ nm), and incomplete desorption of hexanethiol layer between gold nanoparticles that would then act as a dielectric layer.

Organic field effect transistors (OFETs) based on solution processable polymeric semiconductors and conductors have achieved impressive improvements in performance during recent years as an alternative to inorganic semiconductors. These devices have been developed to realize low-cost and large-area electronic products such as active-matrix displays, chemical sensors, and flexible microelectronics on inexpensive polymer substrates.[32] The most popular solution processable materials for electrodes are conducting polymers such as PEDOT/PSS that have intrinsically high resistivity (by 2 or 3 orders higher than metal) and are not desirable for electrodes and interconnect materials for large area or high-quality (high-speed) electronics.[32,33] It is preferred to use metal electrodes and interconnects for high-quality OFET structures on polymer devices. However, low-temperature metal deposition methods that do not require photolithography, or vacuum processes, but are nevertheless capable of producing high resolution are not yet well developed. In this

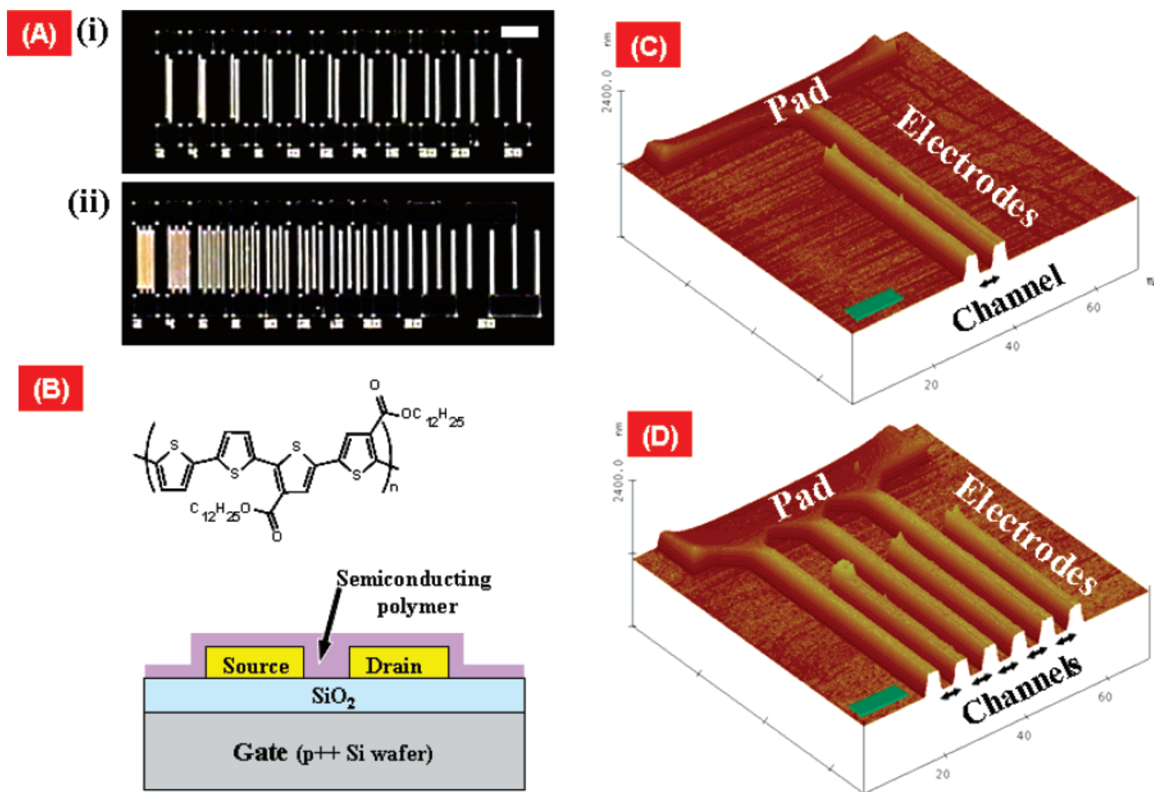

Figure 6. Nanoimprinted OFET with air-stable semiconducting polymer. (A) Optical dark field images of (i) single and (ii) multichannel transistors. Inset scale bar corresponds to 100 μm. (B) Schematics of OFET. Top inset is the graphic formula of air-stable carboxylate-functionalized polythiophene semiconducting polymer. AFM topography image of (C) a single channel OFET and (D) a multiple channel OFET with big contact pads. Inset scale bar corresponds to 10 μm.

respect, the present direct nanoimprinting process of metal nanoparticle solutions enables inexpensive, yet high-resolution metal electrodes for OFET applications.

The OFETs fabricated in this work have a typical bottom gate/bottom contact coplanar transistor configuration (Figure 6B) wherein the channel length is defined by the separation between the two parallel electrodes (source and drain) on top of the SiO_2/P+ Si wafer gate. Carboxylate-functionalized polythiophene (Figure 6B top inset) with increased air stability[34] was synthesized, dissolved in warm (>45 °C) 1,2-dichlorobenzene (*o*-DCB) solvent (3 mg/mL) and spin coated as an active layer. The semiconducting polymer synthesis can be found in the Supporting Information.

Two types of transistor test configurations—single channel transistors shown in Figure 6A, part i (optical dark field image), and Figure 6C (AFM topography) and multiple channel transistors shown in Figure 6A, panel ii (optical dark field image) and Figure 6D (AFM topography)—were fabricated by direct nanoimprinting. Figure 6A shows single channel transistors with various channel lengths (Figure 6B, part i, 2/4/6/8/10/12/16/20/30/50 μm from left) and 160 μm channel width and multiple channel transistors with longer effective channel width (Figure 6B, part ii, 800 μm for 2−6 μm channel and 480 μm for 8−50 μm channel) with same channel length.

The SiO_2/P+ Si wafer was cleaned by piranha solution and dehydrated at 120 °C for 10 min. Au nanoparticles were then nanoimprinted on this substrate. After the nanoimprinted nanoparticles were melted at 140 °C, the air-stable carboxylate-functionalized polythiophene semiconducting polymer was spin coated (10−20 nm thickness) and annealed at 120 °C on a hot plate for 3 min. Figure 6C shows an AFM topography image of a single channel OFET where two vertical lines separated by a narrow channel are source and drain electrodes and the big pad at the end of the narrow line is for probing. Note the very clean and precise, short channel production by nanoimprinting. The AFM images show that the source and drain electrode patterns were replicated precisely and cleanly with no visible residues of Au nanoparticles. This eliminates the need of additional wet etching of Au nanoparticle residues before usage as OFET electrodes.

The sensitivity of conventional organic semiconducting polymers to air necessitates severe precautions during semiconducting polymer material processing, device fabrication and characterization that are usually carried out either in vacuum or in a nitrogen environment. However, air-free environment adds to the cost of manufacturing, thus offsetting advantages of the hybrid inkjet direct writing process that is meant to eliminate vacuum requirements.[34] The air-stable semiconducting polymer used in this research is a novel material of a modified polythiophene containing electron-withdrawing alkyl carboxylate substituents, exhibiting high charge mobility.[35] Due to the electron-withdrawing properties of the carboxylate substituents, the polymer has lower HOMO (highest occupied molecular orbital) energy

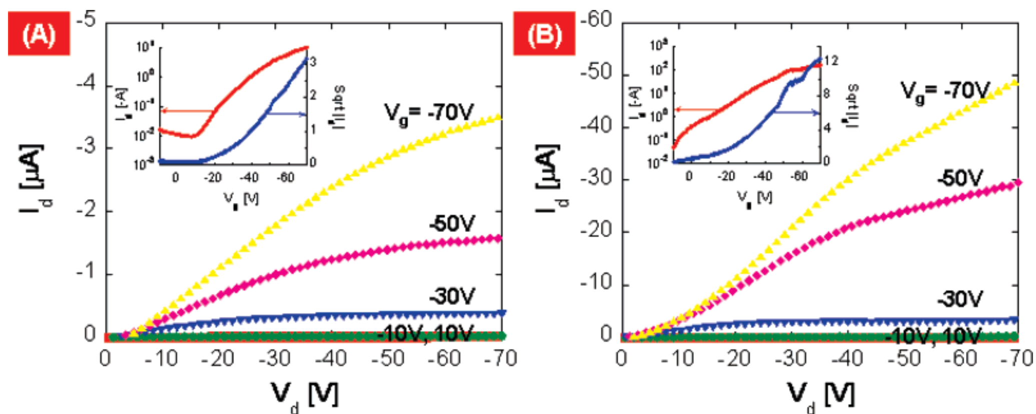

Figure 7. Output and transfer characteristics of OFET with long channel (A, $L \sim 4$ μm) and short channel (B, $L \sim 800$ nm) with 160 μm channel width. For output characteristics measurement, the drain voltage (V_d) was scanned from 0 to -70 V and the drain current (I_d) was measured while gate voltage (V_g) was fixed at -70, -50, -30, -10, 10 V during each V_d scanning. For transfer characteristics measurement (insets), V_g was scanned from 10 to -70 V and the drain current (I_d) was measured while V_d was fixed at -70 V.

levels and therefore provides better oxidative doping stability than conventional solution-processable polythiophenes such as P3HT.[34]

The OFETs performance was characterized using a HP4155A semiconductor parameter analyzer and a probe station with the micropositioning manipulators in a dark Faraday cage in air. The transfer and output characteristics of the OFETs are shown in Figure 7 for different channel lengths. The OFET with relatively longer channel (Figure 7A, $L \sim 4$ μm, $W \sim 160$ μm) shows typical output and transfer characteristics for operation in p-type accumulation mode with I_{on}/I_{off} ratio of 10^3-10^4 and threshold voltage (V_t) of -25 V while the OFET with relatively shorter channel (Figure 7B, $L \sim 800$ nm, $W \sim 160$ μm) exhibited output characteristics with similar I_{on}/I_{off} ratio, but without current saturation, lower threshold voltage (V_t) of -15 V, and much larger drain current. This so-called short channel effect is caused by several reasons.[36] The mobility extracted from the saturated transfer characteristics[36] of the OFET was found to be around 0.004−0.006 $cm^2/V\cdot s$. The nanoparticle nanoimprinting can produce very short channels (micrometer to submicrometer) with high drain current. The resolution of the fabricated OFET is determined by the original mold. Even submicrometer channels could be defined with a nanomold fabricated by e-beam lithography to achieve reduction of the channel length to improve switching speed.

In order to compare the OFET performance, reference devices on a thermally grown SiO_2 (115 nm)/P+ silicon wafer were fabricated by conventional photolithography and vacuum metal deposition process, and the same semiconducting polymer was spin coated under the same condition. The overall performance of the lithographically processed OFET with SiO_2 dielectric layer exhibited similar performance with the imprinted OFETs. This confirms that nanoparticle nanoimprinting can produce similar quality OFETs as conventional photolithography. The OFET performance can be significantly enhanced by the polymer processing optimization or by applying higher mobility semiconducting polymer. Direct nanoimprinting utilizes a fully additive method to form electrodes with the desired width and density. It is also worth mentioning that this is accomplished without using expensive photolithographic methods once the nanoimprinting mold is available.

In conclusion, we have successfully demonstrated that direct nanoimprinting of metal nanoparticles enables low-temperature metal deposition as well as high-resolution patterning. Nano- to microscale features with a wide range of geometries and dimensions were successfully fabricated by nanoimprinting. Our approach thus has substantial potential to take advantage of nanoimprinting for the application in ultralow cost, large area printed electronics. Combined with an air-stable carboxylate-functionalized polythiophene, all solution-processed OFETs with micrometer to submicrometer critical feature resolution were fabricated in a fully maskless sequence, eliminating the need for lithographic processes. All processing and characterization steps were carried out at low temperature and ambient environment, which will enable further applications to electronics on flexible substrates.

Acknowledgment. Financial support to the University of California, Berkeley, by the U.S. National Science Foundation (grant nos. CTS-0417563 and CMMI 0700827), the U.S. Department of Energy (DE-AC03-76SF00098), and Center for Nanoscale Mechatronics and Manufacturing (Grant No. 019997), one of the 21st Century Frontier Research Programs from the Ministry of Science and Technology, Republic of Korea, is gratefully acknowledged.

Supporting Information Available: Synthetic procedures and device fabrication methods. This information is available free of charge via the Internet at http://pubs.acs.org.

References

(1) Trucskett, V. N.; Watt, M. P. C. *Trends Biotechnol.* **2006**, *24* (7), 312−317.
(2) Nakamatsu K.; Matsui, S. *Jpn. J. Appl. Phys.* **2006**, *45* (21), L546−548.
(3) Seekamp, J.; Zankovych, S.; Helfer, A. H.; Maury, P.; Sotomayor Torres, C. M.; Boettger, G.; Liguda, C.; Eich, M.; Heidari, B.; Montelius, L.; Ahopelto, J. *Nanotechnology* **2002**, *13* (5), 581−586.

(4) Wu, W.; Jung, G.-Y.; Olynick, D.; Straznicky, J.; Li, Z.; Li, X.; Ohlberg, D.; Chen, Y.; Wang, S.-Y.; Liddle, J.; Tong, W.; Williams, R. S. *Appl. Phys. A* **2005**, *80* (6), 1173−1178.
(5) Kim, C.; Stein, M.; Forrest, S. R. *Appl. Phys. Lett.* **2002**, *80*, 4051−4053.
(6) Clavijo-Cedeño, C.; Seekamp, J. A.; Kam, P.; Hoffmann, T.; Zankovych, S.; Sotomayor Torres, C. M.; Menozzi, C.; Cavallini, M.; Murgia, M.; Ruani, G.; Biscarini, F.; Behl, M.; Zentel, R.; Ahopelto, J. *Microelectron. Eng.* **2002**, *61−62*, 25−31.
(7) Wu, W.; Cui, B.; Sun, X. Y.; Zhang, W.; Zhunag, L.; and Chou, S. Y. *J. Vac. Sci. Technol., B* **1998**, *16*, 3825−3829.
(8) Chou, S. Y.; Krauss, P. R.; Renstrom, P. J. *Science* **1996**, *272*, 85−87.
(9) Haisma, J.; Verheijen, M.; van der Heuvel, K.; van der Berg, J. *J. Vac. Sci. Technol., B* **1996**, *14*, 4124−4128.
(10) Colburn, M.; Johnson, S.; Stewart, M.; Damle, S.; Bailey, T.; Choi, B.; Wedlake, M.; Michaelson, T.; Sreenivasan, S. V.; Ekerdt, J.; Willson, C. G. *Proc. SPIE* **1999**, *3676*, 379−389.
(11) Sotomayor Torres, C. M. *Alternative Lithography*; Springer: New York, 2003.
(12) Schift, H.; Heyderman, L. J.; Auf der Maur, M.; Gobrecht, J. *Nanotechnology* **2001**, *12*, 173−177.
(13) Yoshihiko, H.; Toshihiko, U.; Tomohiro, K.; Takashi, M. *Proc. SPIE* **2003**, *5220*, 74−81.
(14) Chen, H. L.; Chuang, S. Y.; Cheng, H. C.; Lin, C. H.; Chu, T. C. *Microelectron. Eng.* **2006**, *83*, 893−896.
(15) Heyderman, L. J.; Schift, H.; David, C.; Gobrecht, J.; Schweizer, T. *Microelectron. Eng.* **2000**, *54* (3−4), 229−245.
(16) Sirringhaus, H.; Kawase, T.; Friend, R. H.; Shimoda, T.; Inbasekaran, M.; Wu, W.; Woo, E. P. *Science* **2000**, *290*, 2123−2126.
(17) Chung, J.; Ko, S.; Bieri, N. R.; Grigoropoulos, C. P.; Poulikakos, D. *Appl. Phys. Lett.* **2004**, *84*, 801−803.
(18) Chung, J.; Bieri, N. R.; Ko, S.; Grigoropoulos, C. P.; Poulikakos, D. *Appl. Phys. A* **2004**, *79*, 1259−1261.
(19) Bao, Z.; Feng, Y.; Dodavalapur, A.; Raju, V. R.; Lovinger, A. J. *Chem. Mater* **1997**, *9*, 1299−1301.
(20) Piqué, A.; Chrisey, D. B.; Fritz-Gerald, J. M.; McGill, R. A.; Auyeng, R. C. Y.; Wu, H. D.; Lakeou, S.; Nguyen, V.; Chung, R.; Duiganan, M. *J. Mater. Res.* **2000**, *15*, 1872−1875.
(21) Blanchet, G. B.; Loo, Y. L.; Rogers, J. A.; Gao, F.; Fincher, C. R. *Appl. Phys. Lett.* **2003**, *82*, 463−465.
(22) Buffat, P. A.; Borel, J. P. *Phys. Rev. A* 1976, *13*, 2287−2298.
(23) Ko, S.; Choi, Y.; Hwang, D. J.; Grigoropoulos, C. P.; Poulikakos, D. *Appl. Phys. Lett.* **2006**, *89*, 141126−141128.
(24) Hostetler, M. J.; Wingate, J. E.; Zhong, C. J.; Harris, H. E.; Vachet, R. W.; Clark, M. R.; Nondono, J. D.; Green, S. J.; Stokes, J. J.; Wignall, G. D.; Glish, G. L.; Porter, M. D.; Evans, N. D.; Murray, R. W. *Langmuir* **1998**, *14* (1), 17−30.
(25) Kim, E.; Xia, Y.; Zhao, X.; Whitesides, G. M. *Adv. Mater* **1997**, *9*, 651−654.
(26) Kljan, R.; Bishop, J. M.; Fialkowski, M.; Paszewski, M.; Campbell, C. J.; Gray, T. P.; Grzybowski, B. A. *Science* **2007**, *316*, 261−264.
(27) Reddy, S.; Schunk, P. R.; Bonnecaze, R. T. *Phys. Fluid* **2005**, *17*, 122104(1−6).
(28) Johnson, S.; Burns, R.; Kim, E. K.; Dickey, M.; Schmid, G.; Meiring, J.; Burns, S.; Willson, C. G.; Convery, D.; Wei, Y.; Fejes, P.;Gehoski, K.; Mancini, D.; Nordquist, K.; Dauksher, W. J.; Resnick, D. J. *J. Vac. Sci. Technol., B* **2005**, *23* (6), 2553−2556.
(29) Scheer, H. C.; Schulz, H. *Microelectron. Eng.* **2001**, *56*, 311−332.
(30) Park, I.; Cheng, J.; Pisano, A. P.; Lee, E.; Jeong, J. *Appl. Phys. Lett.* **2007**, *90*, 093902(1−3).
(31) de Gennes, P. G.; Brochard-Wyart, F.; Quere, D. *Capillarity and wetting phenomena*; Springer: NewYork, 2004.
(32) Zschieschang, U.; Klauk, H.; Halik, M.; Schmid, G.; Dehm, C. *Adv. Mater.* **2003**, *15*, 1147−1151.
(33) Burns, S. E.; Cain, P.; Mills, H.; Wang, J.; Sirringhaus, H. *MRS Bull.* **2003**, Nov, 829−834.
(34) Murphy, A. R.; Liu, J.; Luscombe, C.; Kavulak, D.; Frechet, J. M. J.; Kline, R. J.; McGehee, M. D. *Chem. Mater.* **2005**, *17*, 4892−4899.
(35) Ko, S.; Pan, H.; Grigoropoulos, C. P.; Luscombe, C.; Frechet, J. M. J.; Poulikakos, D. *Appl. Phys. Lett.* **2007**, *90*, 141103(1−3).
(36) Pierret, R. F. *Semiconductor Device Fundamentals*; Addison Wesley: New York, 1996.
(37) The melting temperatures as a function of the particle radius are calculated from $\ln T^0/T_M = -(2/\rho_s L)(\rho_s/\rho_l)^{1/3} 1/r_s^* \{\sigma_l(1 - \rho_s/\rho_l) + \sigma_{sl}[1 - \delta/r_s^*(\rho_s/\rho_l)^{1/3}]^{-1}\}$ where σ_{sl} is the solid−liquid interfacial tension, σ_l is the surface tension of the liquid, δ is the liquid-layer thickness, r_s^* is the radius of the particle at the melting point assuming that the particle is in the solid form, ρ_s and ρ_l are the solid and liquid densities, respectively, and L is the latent heat of fusion. The parameters (σ_{sl}, σ_l, ρ_s, ρ_l, L) correspond to the experimental values of bulk gold[38] while δ and σ_{sl} are the same as those obtained in Buffat and Borel[22] fitting their experimental data.
(38) Arcidiacono, S.; Bieri, N. R.; Poulikakos, D.; Grigoropoulos, C. P. *Inter. J. Multiphase Flow* **2004**, *30*, 979−994.

NL070333V